JOURNAL OF THE AMERICAN CHEMICAL SOCIETY

pubs.acs.org/JACS

Article

Cubic Stuffed-Diamond Semiconductors $LiCu_3TiQ_4$ (Q = S, Se, and Te)

Michael A. Quintero, Jiahong Shen, Craig C. Laing, Christopher Wolverton, and Mercouri G. Kanatzidis*

Cite This: *J. Am. Chem. Soc.* 2022, 144, 12789−12799

Read Online

ACCESS | Metrics & More | Article Recommendations | Supporting Information

ABSTRACT: Lithium chalcogenides have been understudied, owing to the difficulty in managing the chemical reactivity of lithium. These materials are of interest as potential ion conductors and thermal neutron detectors. In this study, we describe three new cubic lithium copper chalcotitanates that crystallize in the $P\bar{4}3m$ space group. $LiCu_3TiS_4$, a = 5.5064(6) Å, and $LiCu_3TiSe_4$, a = 5.7122(7) Å, represent two members of a new stuffed diamond-type crystal structure, while $LiCu_3TiTe_4$, a = 5.9830(7) Å crystallized into a similar structure exhibiting lithium and copper mixed occupancy. These structures can be understood as hybrids of the zinc-blende and sulvanite structure types. In situ powder X-ray diffraction was utilized to construct a "panoramic" reaction map for the preparation of $LiCu_3TiTe_4$, facilitating the design of a rational synthesis and uncovering three new transient phases. $LiCu_3TiS_4$ and $LiCu_3TiSe_4$ are thermally stable up to 1000 °C under vacuum, while $LiCu_3TiTe_4$ partially decomposes when slowly cooled to 400 °C. Density functional theory calculations suggest that these compounds are indirect band gap semiconductors. The measured work functions are 4.77(5), 4.56(5), and 4.69(5) eV, and the measured band gaps are 2.23(5), 1.86(5), and 1.34(5) eV for the S, Se, and Te analogues, respectively.

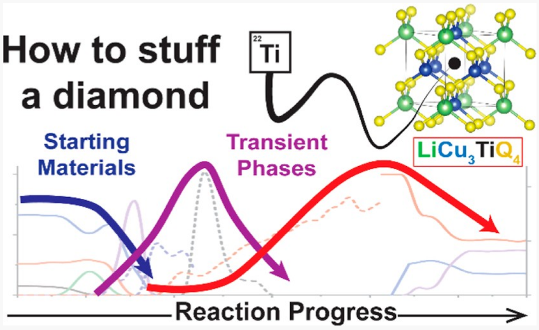

INTRODUCTION

The discovery of new inorganic materials is necessary for continued scientific and technological advancements. New lithium-based materials have the potential to bring forth new candidates with fundamental promise for applications, including both energy storage[1] and direct capture neutron detector[2] technologies. In the case of batteries, mobile Li atoms are used to dispense energy on demand for consumption.[3] In contrast, the detection of thermal neutrons relies on the immobility of Li atoms which combine with incident neutrons during the direct capture detection process.[2,4] Evidence of this fact can be found in the recent reports of the novel materials $LiInP_2Se_6$ and $LiInSe_2$ and their outstanding neutron detecting performance, performance that was previously unattainable with existing materials.[4,5]

So-called "stuffed" diamond compounds exhibit an identifiable diamond sublattice with at least one additional atom added to the structure. Stuffed diamond compounds can be categorized as either cubic if the sublattice has the aristotype zinc-blende structure or hexagonal if the sublattice has a wurtzite structure. The half-heusler[6] family of compounds (with general formula XYZ) is perhaps the best studied family of stuffed diamond compounds, falling into the cubic variety. Members of this family have been investigated as topological insulators,[7,8] superconductors,[9−12] and thermoelectric materials.[13−15] Typical compositions seen in stuffed diamond compounds include transition metals (e.g., TiNiSi),[16,17] lanthanides (e.g., YbSnBi),[17,18] and main group[17,19,20] elements (e.g., GbNiGa and GbNiIn) up to and including the pnictides (e.g., CaAgP and CaAgAs).[21] However, reports of stuffed diamond compounds containing lithium atoms are less common. Examples in the literature, including the intermetallic phases of $Li_3Zn_2Sn_4$,[22] Li_2ZnGe_3,[22] Li_2AgGe,[23] and $Li_{2.53}AgGe_2$,[23] can be considered stuffed hexagonal diamond compounds because their structures exhibit wurtzite sublattices. However, little is known about the properties of semiconducting lithium-containing stuffed diamond compounds, which serve as motivation for the search for new stuffed diamond chalcogenides.

A structure closely related to the cubic stuffed diamond structures is that of sulvanite with the general formula Cu_3MQ_4 (M = V, Nb, and Ta; Q = S, Se, and Te).[24,25] This family of materials has received significant interest for applications in photocatalytic water splitting[25,26] and thermoelectrics,[27−29] among others. Recently, the thermoelectric properties of the

Received: April 2, 2022
Published: July 7, 2022

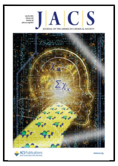

ACS Publications

compound Cu_4TiSe_4, a sulvanite and zinc-blende derivative, were experimentally measured and found to have room-temperature thermal conductivity of 0.19 W m^{-1} K^{-1}.[30] The origin of the low thermal conductivity in Cu_4TiSe_4 is ascribed, in part, to loosely bound Cu atoms in the structure that serve as "intrinsic rattlers."[30]

In this study, we describe the synthesis, crystal structures, and properties of three stable new cubic lithium copper chalcotitanates with the general formula $LiCu_3TiQ_4$ (Q = S, Se, and Te). Additionally, panoramic synthesis was employed for the preparation of $LiCu_3TiTe_4$. The compounds $LiCu_3TiS_4$ and $LiCu_3TiSe_4$ are isostructural and crystallize in a cubic 3D stuffed diamond structure that can be considered a combination of the zinc-blende and sulvanite types, distinct from the Cu_4TiSe_4 crystal structure. $LiCu_3TiTe_4$ crystallizes in a structure related to $LiCu_3TiS_4$ but closer to the sulvanite structure type and exhibits mixed occupation between Li and Cu at two different sites. Density functional theory (DFT) calculations predict indirect band gaps and hole carriers with lower effective masses than electrons.

■ EXPERIMENTAL SECTION

Reagents and Synthesis. All starting elements except for Cu were used as obtained: sulfur buttons S (99.99%, 5N Plus Inc., Saint-Laurent, Quebec, Canada), Se (99.99% American Elements), Te (99.99% American Elements), Ti powder −325 mesh (99.9% Sigma-Aldrich), Li sticks (99.9% Sigma-Aldrich), and Cu powder −100 mesh (99% Alfa Aesar). Li_2Q (Q = S, Se, and Te) was prepared using condensed ammonia, as reported previously.[31]

Activation of the Cu Powder. Cu powder was placed into a fine-frit funnel and washed with a 10 wt % (3.3 M) aqueous solution of HCl while being stirred with a plastic spatula, and thereafter vacuum filtered to remove the solution. This process was repeated until the color of the Cu powder remained pink/red (approximately three times in our case). The activated Cu powder was then washed once with deionized water, filtered, washed once with isopropyl alcohol, and filtered again. The finished product was then pumped into an N_2 glovebox overnight for storage.

Synthesis of $LiCu_3TiS_4$. The phase pure powder was synthesized by reacting stoichiometric amounts 2.408 mmol (153.0 mg) activated Cu powder, 0.802 mmol (38.4 mg) Ti powder, 2.81 mmol (90.1 mg) ground S, and 0.400 mmol (18.4 mg) Li_2S powder massed in a nitrogen double glovebox. The S, Ti, and Li_2S were ground together in an agate mortar pestle until a homogeneous mixture was obtained. Because of the mechanochemical reaction that occurs between sulfur and copper,[32] care must be taken when combining them in a mortar and pestle; otherwise, the reaction will proceed quickly, resulting in the vaporization of some sulfur before the reagents can be placed in a crucible. With this in mind, the Cu powder was then added to the mortar with the other ground reagents and mixed using a piece of weighing paper. It was left to sit undisturbed for ∼30 min, remixed with a piece of weighing paper, left to sit undisturbed for an additional ∼30 min, and finally ground gently with a pestle. When first combined, the powder appeared yellow/white in color but as it was left to sit, the color slowly changed to dark gray as the Cu and S slowly reacted. The homogenized powder was then loaded into a stainless-steel die and pressed into a cylindrical pellet with a diameter of 6 mm using a vise to apply the pressing force. The pressed pellet was then placed into a glassy carbon crucible, which was then placed into an 18 mm outer and 16 mm inner diameter fused-silica tube. The fused-silica tube, containing the pellet and crucible, was then evacuated to $\sim 4 \times 10^{-3}$ mbar and flame sealed so that the final length of the tube was ∼13 cm. The sealed tube was then loaded into a vertical tube furnace such that the top of the tube was below the middle of the furnace, and the tip of the thermocouple was at the same depth as the crucible. The tube was then heated to 600 °C at a rate of 50 °C/h, soaked at 600 °C for 10 h, and then allowed to cool to room temperature by turning off the furnace. The sealed tube was opened in an N_2 glovebox, and the pellet was hand ground in an agate mortar and pestle. The reground powder was then pressed into a pellet with a diameter of 6 mm and placed in the same glassy carbon crucible. The crucible was then loaded into an 18 mm outer and 16 mm inner diameter fused-silica tube, evacuated to $\sim 4 \times 10^{-3}$ mbar, and flame sealed. The sealed tube was then placed in a vertical tube furnace, heated to 600 °C at a rate of 50 °C/h, and soaked at 600 °C for 24 h, after which the furnace was turned off, and the tube was cooled to room temperature. The sealed tube was then pumped into an N_2 glovebox and opened. The samples were stored in an N_2 glovebox. The synthesized powders appeared mustard yellow and were typically phase pure by powder X-ray diffraction (PXRD).

Synthesis of $LiCu_3TiS_4$ Single Crystals. Stoichiometric amounts of 1.40 mmol (88.9 mg) of activated Cu powder, 1.40 mmol (66.9 mg) of Ti powder, 3.410 mmol (112.1 mg) of ground S, and 0.699 mmol (32.1 mg) of Li_2S powder were massed in an N_2 glovebox. Ti, Li_2S, and S were then ground together in an agate mortar and pestle. Cu was then added to this mixture in the manner described above (see the synthesis of $LiCu_3TiS_4$ powder). The homogenized powder was then loaded into a stainless-steel die and pressed into a pellet with a diameter of 6 mm, using a vise to apply the pressing force. The pressed pellet was then placed into a glassy carbon crucible, which were both placed thereafter, into an 18 mm outer and 16 mm inner diameter fused-silica tube. The fused-silica tube, containing the pellet and crucible, was then evacuated to $\sim 4 \times 10^{-3}$ mbar and flame sealed so that the final length of the tube was ∼13 cm. The sealed tube was then loaded into a vertical tube furnace such that the top of the tube was below the middle of the furnace, and the tip of the thermocouple was at the same depth as the crucible. The tube was then heated to 800 °C at a rate of 50 °C/h, soaked at 800 °C for 10 h, cooled to 550 °C at a rate of 12.5 °C/h, after which the furnace was turned off, and the tube was cooled to room temperature. The tube was then brought into an N_2 double glovebox and opened. From the resulting pellet, 100 mg was removed and combined with 0.7029 mmol (32.3 mg) of Li_2S and 2.112 mmol (67.7 mg) of S in an agate mortar and pestle. After grinding until a homogeneous mixture was obtained, the powder was placed into a glassy carbon crucible, which was then placed into an 18 mm outer and 16 mm inner diameter fused-silica tube. The fused-silica tube, containing the powder and crucible, was then evacuated to $\sim 4 \times 10^{-3}$ mbar and flame sealed so that the final length of the tube was ∼13 cm. The sealed tube was then loaded into a vertical tube furnace such that the top of the tube was below the middle of the furnace, and the tip of the thermocouple was at the same depth as the crucible. The tube was then heated to 900 °C at a rate of 50 °C/h, soaked at 900 °C for 24 h, cooled to 450 °C at a rate of 10 °C/h, after which the furnace was turned off, and the tube was allowed to cool to room temperature. The tube was then opened in air, and the product was soaked in ethanol overnight to isolate the crystals. The crystals appeared black with an octahedral morphology. The percentage yield of the reaction was ∼50%.

Synthesis of $LiCu_3TiSe_4$. The powder was synthesized by reacting stoichiometric amounts 1.603 mmol (101.9 mg) of activated Cu powder, 0.535 mmol (25.6 mg) of Ti powder, 1.871 mmol (147.7 mg) of ground Se, and 0.267 mmol (24.8 mg) of Li_2Se powder massed in a nitrogen double glovebox and ground together in an agate mortar and pestle. The homogenized powder was then loaded into a stainless-steel die and pressed into a pellet with a diameter of 6 mm, using a vise to apply the pressing force. The pressed pellet was then placed into a glassy carbon crucible, which were both placed thereafter, into an 18 mm outer and 16 mm inner diameter fused-silica tube. The fused-silica tube, containing the pellet and crucible, was then evacuated to $\sim 4 \times 10^{-3}$ mbar and flame sealed so that the final length of the tube was ∼13 cm. The sealed tube was then loaded into a vertical tube furnace such that the top of the tube was below the middle of the furnace, and the tip of the thermocouple was at the same depth as the crucible. The tube was then heated to 600 °C at a rate of 50 °C/h, soaked at 600 °C for 10 h, and then cooled to room temperature by turning off the furnace. The sealed tube was then pumped into an N_2 glovebox, the tube was opened, and the pellet was ground in an agate mortar and pestle. The reground powder was then pressed into a pellet with a diameter of 6 mm and placed into the same glassy carbon crucible. The crucible was then loaded into an 18 mm outer and 16 mm inner diameter fused-silica tube, evacuated to ∼4×10^{-3} mbar, and flame sealed. The sealed tube was then placed in a vertical tube furnace, heated to 600 °C at a rate of 50 °C/h, soaked at 600 °C for 24 h, after which the furnace was turned off, and the tube was allowed to cool to room temperature. The sealed tube was then pumped into an N_2 glovebox, where it was opened, and the sample was stored. The synthesized powders appeared gray/black and typically exhibited a small $TiSe_2$ impurity, as determined by PXRD.

Synthesis of $LiCu_3TiSe_4$ Single Crystals. Stoichiometric amounts of 0.4375 mmol (27.8 mg) of activated Cu powder, 0.4387 mmol (21.0 mg) of Ti powder, 2.4088 mmol (190.2 mg) of ground Se, and 0.6570 mmol (61.0 mg) of Li_2Se powder were massed in a nitrogen double glovebox and ground together in an agate mortar and pestle. The ground powder was placed into a glassy carbon crucible, which was loaded into an 18 mm outer and 16 mm inner diameter fused-silica tube. The tube was then removed from the glovebox, evacuated to ∼2×10^{-3} mbar, and flame sealed. The sealed tube was then placed into a vertical tube furnace, heated to 900 °C at a rate of 50 °C/h, soaked at 900 °C for 24 h, cooled to 450 °C at a rate of 10 °C/h, after which the furnace was turned off, and the tube was cooled to room temperature. The tube was then opened in air, and the product in the crucible was soaked in ethanol overnight. The crystals appeared black with an octahedral morphology. The percentage yields were typically ∼35%.

Synthesis of $LiCu_3TiTe_4$. The synthesis of powder was achieved by reacting stoichiometric amounts 1.19 mmol (75.7 mg) of activated Cu powder, 0.397 mmol (19.0 mg) of Ti powder, 1.389 mmol (177.3 mg) of ground Te, and 1.20 mmol (28.1 mg) of Li_2Te powder massed in a nitrogen double glovebox and ground together in an agate mortar and pestle. The homogenized powder was then loaded into a stainless-steel die and pressed into a pellet with a diameter of 6 mm, using a vise to apply the pressing force. The pressed pellet was then placed into a glassy carbon crucible, which were both placed thereafter, into an 18 mm outer and 16 mm inner diameter fused-silica tube. The fused-silica tube, containing the pellet and crucible, was then evacuated to ∼4×10^{-3} mbar and flame sealed so that the final length of the tube was ∼13 cm. The sealed tube was then loaded into a vertical tube furnace such that the top of the tube was below the middle of the furnace, and the tip of the thermocouple was at the same depth as the crucible. The tube was then heated to 450 °C at a rate of 50 °C/h, soaked at 450 °C for ∼4 h, and then water quenched. Successful synthesis of the compound yielded black powder with a small CuTe impurity, as determined by PXRD.

Synthesis of $LiCu_3TiTe_4$ Single Crystals. The amounts of 1.718 mmol (109.2 mg) of activated Cu powder, 0.572 mmol (76.9 mg) of Ti powder, 2.005 mmol (255.9 mg) of ground Te, 0.286 mmol (40.5 mg) of Li_2Te, and 5.730 mmol (766.9 mg) of LiI powder massed in a nitrogen double glovebox and ground together in an agate mortar and pestle. The powder was then placed into a glassy carbon crucible, which was then loaded into an 18 mm outer and 16 mm inner diameter fused-silica tube. The tube was removed from the glovebox, evacuated to ∼4×10^{-3} mbar, and then flame sealed so that the final length of the tube was ∼13 cm. The sealed tube was then loaded into a vertical tube furnace such that the top of the tube was below the middle of the furnace, and the tip of the thermocouple was at the same depth as the crucible. The tube was then heated to 1000 °C at a rate of 50 °C/h, soaked at 1000 °C for 24 h, and slowly cooled to 570 °C at a rate of 10 °C/h, after which the furnace was turned off, and the tube was allowed to cool to room temperature. The tube was then opened in an N_2 glovebox, where the sample was stored. The crystals were black with an octahedral morphology. The percentage yields were typically ∼35%.

In Situ Powder X-ray Diffraction of $LiCu_3TiTe_4$. A STOE STADI MP high-resolution diffractometer with an oven attachment (STOE HT) was used to collect temperature-dependent data. The diffractometer was equipped with an asymmetric curved germanium monochromator and a one-dimensional silicon strip detector (MYTHEN2 1K from DECTRIS). The starting materials were combined, as described in the section "Synthesis of $LiCu_3TiTe_4$ powder," packed into a 0.7 mm diameter fused-quartz capillary which was then evacuated to ∼3×10^{-3} mbar, and flame sealed. All capillaries were carbon coated to prevent glass attacks. Ground fused-silica powder was added to each capillary to protect the tip of the capillary, which could not be coated with carbon. Data were collected using pure-Ag Kα1 radiation (0.559407 Å) operated at 40 kV and 40 mA. Temperature stability is typically 0.1 °C. The samples were spun during the collection. The heating profile used during collection is shown in Figure S4.

Density Functional Theory. In this study, all DFT[33,34] calculations were performed using the Vienna ab initio simulation package[35,36] and the projector augmented wave[37] method. The Perdew−Burke−Ernzerhof[37−39] generalized gradient approximation was used as the exchange-correlation functional. A plane wave basis set with a cutoff energy of 650 eV was adopted, and a Γ-centered k-point grid of 10 × 10 × 10 was used to sample the Brillouin zone for the primitive cell of $LiCu_3TiS_4$ and $LiCu_3TiSe_4$ (nine atoms). The structures were fully relaxed until the total energy converged to 10^{-8} eV and the force on each atom was less than 0.001 eV/Å. Phonon calculations were performed with a 2 × 2 × 2 supercell using the Phonopy package.[40]

Photoemission Yield Spectroscopy in Air. A Riken-Keiki AC-2 instrument was used to perform photoemission yield spectroscopy in air (PYSA). Photoelectrons were generated by illuminating the sample with a tunable monochromatic ultraviolet light (UV, 4.2−6.2 eV) under dry air. At each excitation energy, photoelectrons are generated only when the photon energy is higher than the work function. For a semiconductor, this is equal to the valence band maxima (VBM) with respect to the vacuum energy. Extrapolation of the linear region of the data gives the onset of the PYSA spectra, which is the work function.

RESULTS AND DISCUSSION

Synthesis and Stability. $LiCu_3TiS_4$ and $LiCu_3TiSe_4$ can be readily synthesized via a direct combination of the elements with Li_2Q (Q = S and Se) as the Li source. $LiCu_3TiS_4$ can be prepared with no observable secondary phases (see Figure 1a), while $LiCu_3TiSe_4$ formed with a small amount of $TiSe_2$ as a secondary phase (see Figure 1b). The use of two separate reaction steps instead of one longer annealing step was used to prepare the sulfur and selenide analogues to primarily ensure good mixing of the reagents as the pellet expands considerably (∼4× in height) after the first heating step. Attempts to synthesize $LiCu_3TiTe_4$ using the same conditions predominantly yielded the targeted phase with Te and CuTe as impurities. Scanning electron microscopy (SEM) images and energy-dispersive X-ray spectroscopy (EDX) spectra confirmed the presence of all reagents close to their target compositions (Figures S1 and S2). An investigation of the reaction progress via in situ panoramic X-ray diffraction study (Figure 2a) was conducted using the temperature profile depicted in Figure S4 to investigate the time sequence in the formation of these intermediate impurities.[41−44] This profile was selected to closely mimic the synthetic conditions used in the ex situ reactions. The results of this experiment are summarized in Figure 2b, where phase wt fractions were determined via multiphase Rietveld refinements in the program GSAS-II.[45] The intensity of the strongest reflection in each phase was tracked for the phases that could not be included in the structure refinements.

From this experiment, we learned the following: between 25 °C and 100 °C, all starting reagents were present and only thermal expansion was observed. From 125 to 200 °C, Li_2Te reacts with the available Te to form $LiTe_3$, completely consuming all the Li_2Te at 200 °C. The intensity of $LiTe_3$

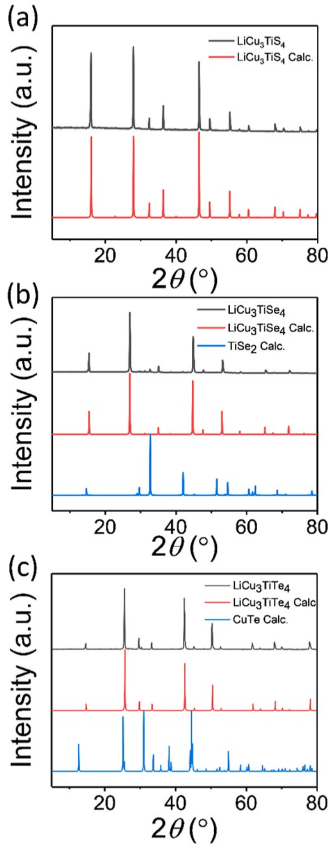

Figure 1. (a) Comparison of the as-synthesized $LiCu_3TiS_4$ against the theoretical pattern, (b) comparison of the as-synthesized $LiCu_3TiSe_4$ against the theoretical pattern, with $TiSe_2$ secondary phase calculated pattern, and (c) comparison of the as-synthesized $LiCu_3TiTe_4$ against the theoretical pattern, with CuTe secondary phase calculated pattern.

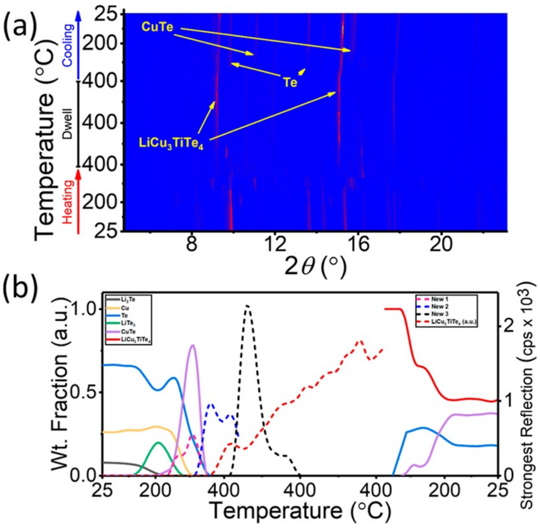

Figure 2. (a) In situ PXRD of reaction progress for the synthesis of $LiCu_3TiTe_4$ collected using Ag Kα1 radiation (0.559407 Å) and (b) reaction evolution plot constructed using Rietveld refined wt. fractions (left axis) and the intensity of the strongest reflection (right axis) for phases that could not be included in refinements.

appears to peak at 200 °C, beginning to decrease by 225 °C, until it was no longer visible at 300 °C. At 225 °C, we first observed the formation of CuTe, which continued to grow in intensity until it was consumed between 320 and 340 °C. We also observed the initial formation of the target phase, $LiCu_3TiTe_4$, at 225 °C. Accordingly, the amount of Cu metal began to decrease, beginning at 225 °C until it was fully consumed at 320 °C. In addition, at 225 °C, we observed the formation of an unidentified intermediate phase termed New-1, which grew until 275 °C, before abruptly disappearing at 300 °C. Between 320 and 340 °C, large changes occurred in the phase composition of the reaction. Between these two scans, all CuTe and Te were consumed. Their disappearance was coupled with the appearance of an intermediate phase, New-2, which was then slowly consumed between 340 and 400 °C, giving way to yet another intermediate phase, New-3. Phase New-3 first appeared at 12 min into the 400 °C dwell and saw a sharp rise in both intensity and crystallinity after 18 min. Phase New-3 was fully converted into $LiCu_3TiTe_4$ 108 min into the dwell. Throughout the 400 °C dwell, the two dominant phases were New-3 and $LiCu_3TiTe_4$. As New-3 was consumed, $LiCu_3TiTe_4$ increased in intensity until it was the only observable phase after 126 min. As $LiCu_3TiTe_4$ was cooled from 400 °C, we observed partial decomposition into CuTe at 380 °C, followed by precipitation of Te metal beginning at 320 °C. These three phases are the only ones observed during the cooling segment, and all persisted at room temperature. Using the insight gained from the panoramic experiment, we attempted a more rational synthesis, in which the sample was quenched above the decomposition temperature and found that we could successfully prepare the material (see Figure 1c) close to its targeted composition (see Figure S3).

Differential thermal analysis (DTA) was conducted on all compounds between 30 and 1000 °C, with two heating and cooling cycles per sample. For $LiCu_3TiS_4$, DTA showed one small thermal event at ~800 °C, which appeared during both heating and cooling (see Figure S5). By comparing the pre-and post-DTA PXRD patterns of the sample (see Figure S6), it was determined that $LiCu_3TiS_4$ partially decomposed into $CuTi_2S_4$ and another unidentified phase. The DTA of $LiCu_3TiSe_4$ (see Figure S7) showed two small thermal events at ~350 and ~800 °C. The PXRD after measurements (see Figure S8) confirmed the presence of $Cu_{0.87}Se$ and $TiSe_2$ as secondary phases with $LiCu_3TiSe_4$ as the majority phase. For $LiCu_3TiTe_4$, DTA showed two small thermal events at ~330 and ~680 °C, as shown in Figure S9. The post-DTA powder pattern (see Figure S10) indicated that $LiCu_3TiTe_4$ was the major phase with elemental Te and $Cu_{2.86}Te_2$ as secondary phases. After DTA, visual inspection of all samples suggested that none had melted because the samples had not formed ingots but instead appeared to be sintered powder.

The stability of the compounds in air and in acid was studied as lithium chalcogenides generally react readily under these conditions. We found that all three materials slowly converted into similarly structured phases over several weeks (see Figures S11−S13), which is coupled with the appearance of some new reflections which are yet to be identified. These new phases are characterized by both a reduction in the intensity of the (100) reflection and a slight contraction of the unit cell, with the magnitude of these changes following the trend S > Se > Te. The stability of the materials was further evaluated by exposing them to HCl with pH = 3. After a week in solution, the PXRD patterns for $LiCu_3TiS_4$ and $LiCu_3TiSe_4$ appeared nearly identical to patterns collected on samples that had only been exposed to ambient air for 3 months, see Figures S14 and S15. For $LiCu_3TiTe_4$, the compound partially decomposed into Te

Table 1. Crystal Data and Structure Refinement for $LiCu_3TiQ_4$ (Q = S, Se, and Te)

empirical formula	$LiCu_3TiS_4$	$LiCu_3TiSe_4$	$LiCu_3TiTe_4$
formula weight	373.70	559.38	755.86
temperature	293(2) K	293(2) K	293(2) K
wavelength	0.71073 Å	0.71073 Å	0.71073 Å
crystal system	cubic	cubic	cubic
space group	$P\bar{4}3m$	$P\bar{4}3m$	$P\bar{4}3m$
unit cell dimensions	$a = b = c = 5.5064(6)$ Å $\alpha = \beta = \gamma = 90°$	$a = b = c = 5.7122(7)$ Å $\alpha = \beta = \gamma = 90°$	$a = b = c = 5.9830(7)$ Å $\alpha = \beta = \gamma = 90°$
volume	166.96(5) $Å^3$	186.38(7) $Å^3$	214.17(8) $Å^3$
Z	1	1	1
density (calculated)	3.717 g/cm^3	5.001 g/cm^3	5.860 g/cm^3
absorption coefficient	11.698 mm^{-1}	28.888 mm^{-1}	21.498 mm^{-1}
F(000)	176	248	320
crystal size	0.2 × 0.3 × 0.2 mm^3	0.4 × 0.3 × 0.4 mm^3	0.14 × 0.12 × 0.08 mm^3
θ range for data collection	3.700 to 36.263°	3.567 to 36.403°	3.405 to 76.057°
index ranges	$-7 \leq h \leq 7$ $-9 \leq k \leq 9$ $-7 \leq l \leq 9$	$-9 \leq h \leq 7$ $-9 \leq k \leq 9$ $-9 \leq l \leq 9$	$-16 \leq h \leq 13$ $-15 \leq k \leq 7$ $-16 \leq l \leq 16$
reflections collected	2105	2677	6995
independent reflections	188 [R_{int} = 0.0166]	212 [R_{int} = 0.0296]	919 [R_{int} = 0.0239]
completeness to θ = 25.242°	100%	100%	100%
refinement method	full-matrix least-squares on F^2	full-matrix least-squares on F^2	full-matrix least-squares on F^2
data/restraints/parameters	188/0/10	212/0/10	919/2/14
goodness-of-fit	1.338	1.321	1.162
final R indices [$I > 2\sigma(I)$]	R_{obs} = 0.0301, wR_{obs} = 0.0800	R_{obs} = 0.0423, wR_{obs} = 0.1086	R_{obs} = 0.0245, wR_{obs} = 0.0702
R indices (all data)	R_{all} = 0.0331, wR_{all} = 0.0828	R_{all} = 0.0513, wR_{all} = 0.1379	R_{all} = 0.0261, wR_{all} = 0.0711
extinction coefficient	0.053(12)	0.076(13)	0.0130(19)
largest diff. peak and hole	1.120 and −1.089 $e \cdot Å^{-3}$	1.926 and −1.324 $e \cdot Å^{-3}$	2.970 and −2.433 $e \cdot Å^{-3}$

metal and CuTe, with the major phase showing strong similarities to material exposed only to air. These results suggest that each material, after partial conversion, achieves some stability against further decomposition. SEM and EDS measurements of each material after exposure to acid showed their compositions to be relatively close to the compositions of the title compounds (see Figures S17−S19).

Crystal Structures. The sulfur and selenide compounds crystallize in a "stuffed" diamond structure in the acentric space group $P\bar{4}3m$ (see Table 1), using the general formula $LiCu_3TiQ_4$ (Q = S and Se), which to the best of the authors' knowledge, has yet to be reported (see Figure 3a). It can be constructed using the zinc-blende structure as a starting point, as shown in Figure 3b. The cation sites in the zinc blende are occupied by lithium, sitting on the corners of the unit cell, and copper, sitting on its faces, while the anion sites are fully occupied by the Q ions, where the structure deviates from zinc blende is the addition, or stuffing, of a cation to the body center of the unit cell, which is normally void in the zinc-blende structure. An alternative construction of the structures reported herein can be made using the sulvanite structure as a starting point, as shown in Figure 4b. In sulvanite, Cu_3MQ_4 (M = V, Nb, and Ta; Q = S, Se, and Te), the Cu, M, and Q atoms occupy the same sites as Cu, Ti, and Q in these structures, with

Table 2. Selected Bond Lengths for $LiCu_3TiQ_4$ (Q = S, Se, and Te)

bond	$LiCu_3TiS_4$	$LiCu_3TiSe_4$	bond	$LiCu_3TiTe_4$
Li−Q	2.488(2)	2.5414(15)	$Li_{0.195}Cu_{0.055}$−Q	2.737(4)
Cu−Q	2.3519(7)	2.4516(6)	$Cu_{0.926}Li_{0.074}$−Q	2.6087(3)
Ti−Q	2.281(2)	2.4055(15)	Ti−Q	2.6432(4)

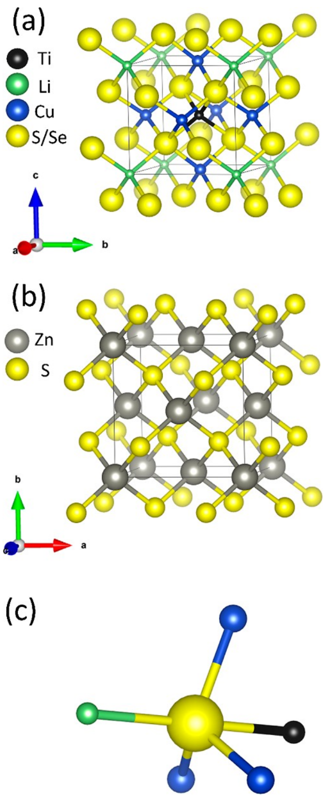

Figure 3. Crystal structures of (a) $LiCu_3TiQ_4$ (Q = S and Se) and (b) zinc blende or sphalerite (ZnS). Local coordination of (c) Q in $LiCu_3TiQ_4$ (Q = S and Se).

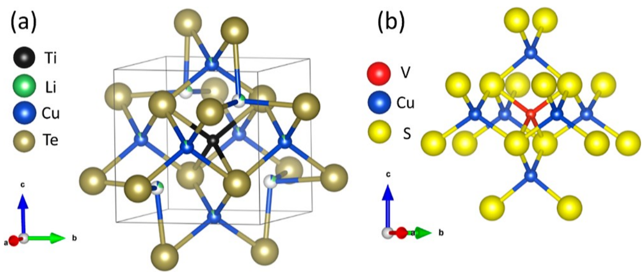

Figure 4. Crystal structures of (a) $LiCu_3TiTe_4$ and (b) sulvanite (Cu_3VS_4).

the main difference being that the Li site is empty. When the sulvanite and zinc-blende structures are combined, we arrive at the $LiCu_3TiQ_4$ (Q = S and Se) structure observed here.

In $LiCu_3TiQ_4$ (Q = S and Se), all the lithium and titanium atoms exhibit slight site mixing between their tetrahedral sites, while the Cu and Q sites are fully occupied with no disorder. The crystal coordinates, occupancies, and thermal parameters are summarized in Tables 3 and 4. The structures were refined by first allowing the Ti occupancy to freely refine with the occupancy of all other atoms fixed to 1, which came to a value less than 1 in both the sulfide and selenide. When Cu and Se were each allowed to freely refine their occupancies, they each converged to values within 0.1% of full occupancy and so were each fixed to a value of 1. The best refinement was then achieved in each structure by linking the occupancies of Li and Ti through a free variable across both tetrahedral sites. The refined formulas for each compound can then be written to emphasize their site occupancy disorder as $(Li_{0.96}Ti_{0.04})Cu_3(Ti_{0.96}Li_{0.04})S_4$ and $(Li_{0.90}Ti_{0.10})Cu_3(Ti_{0.90}Li_{0.10})Se_4$. The metal to Q bond distances for both compounds are summarized in Table 2. The coordination of sulfur and selenium in both these compounds is unique, as shown in Figure 3c, as they bond to three copper atoms and a lithium atom in a tetrahedral arrangement with Ti capping the face formed by the copper atoms to arrive at a coordination number of five. The Li−Q bond distances in the compounds are 2.488(2) Å for the sulfide and 2.5414(15) Å for the selenide. These compare well with the reported Li−Q bond distances in Li_2S,[46] 2.49415(5) Å, and Li_2Se,[47] 2.59868(18) Å, where the slight contraction can be rationalized by the small Ti occupancy present on each site.

Table 3. Atomic Coordinates (×10^4) and Equivalent Isotropic Displacement Parameters (Å^2 × 10^3) for $LiCu_3TiS_4$ at 293(2) K, with Estimated Standard Deviations in Parentheses

label	*x*	*y*	*z*	occupancy	U_{eq}[a]
Li(1)	0	0	0	0.96(2)	39(12)
Li(2)	5000	5000	5000	0.04(2)	8(1)
Cu(1)	0	5000	5000	1	20(1)
Ti(1)	5000	5000	5000	0.96(2)	8(1)
Ti(2)	0	0	0	0.04(2)	39(12)
S(1)	7391(2)	7391(2)	7391(2)	1	14(1)

[a] U_{eq} is defined as one-third of the trace of the orthogonalized U_{ij} tensor.

Table 4. Atomic Coordinates (×10^4) and Equivalent Isotropic Displacement Parameters (Å^2 × 10^3) for $LiCu_3TiSe_4$ at 293(2) K, with Estimated Standard Deviations in Parentheses

label	*x*	*y*	*z*	occupancy	U_{eq}[a]
Li(1)	0	0	0	0.90(4)	35(12)
Li(2)	5000	5000	5000	0.10(4)	15(2)
Cu(1)	0	5000	5000	1	24(1)
Ti(1)	5000	5000	5000	0.90(4)	15(2)
Ti(2)	0	0	0	0.10(4)	35(12)
Se(1)	2569(2)	7431(2)	7431(2)	1	20(1)

[a] U_{eq} is defined as one-third of the trace of the orthogonalized U_{ij} tensor.

The telluride analogue shares the same stoichiometry as the sulfide and selenide. It has a similar structure (see Figure 4a), except that the lithium in the structure occupies a trigonal pyramidal site with 1/4 total occupancy (see Table 5). In addition, the best refinement of the structure indicates mixed occupancy between copper and lithium on this site and the tetrahedral copper site. The refined amounts of copper and lithium were obtained by first allowing for mixed occupancy on both the copper tetrahedral site and the lithium octahedral site. These ratios were then freely refined while being linked to each other to ensure charge neutrality of the compound during refinement. The converged values for the octahedral site gave Li an occupancy of ∼19.4% and copper occupancy of ∼5.6%. In the case of the copper tetrahedral site, the refined occupancy of copper was ∼92.6% and that of lithium was ∼7.4%. The (Li/Cu)−Te bond distance in the compound is 2.737(5) Å, which is slightly shorter than the Li−Te bond distance in Li_2Te[48] 2.82194(5) Å but within the range of the observed Cu−Te distance in $Cu_{1.79}Te$.[49]

Table 5. Atomic Coordinates (×10^4) and Equivalent Isotropic Displacement Parameters (Å^2 × 10^3) for $LiCu_3TiTe_4$ at 293(2) K, with Estimated Standard Deviations in Parentheses

label	*x*	*y*	*z*	occupancy	U_{eq}[a]
Li(1)	7902(8)	7902(8)	7902(8)	0.1946(6)	15(1)
Li(2)	5000	5000	0	0.0739(8)	18(1)
Cu(1)	5000	5000	0	0.9261(8)	18(1)
Cu(2)	7902(8)	7902(8)	7902(8)	0.0554(6)	15(1)
Ti(1)	5000	5000	5000	1	12(1)
Te(1)	7551(1)	7551(1)	2449(1)	1	15(1)

[a] U_{eq} is defined as one-third of the trace of the orthogonalized U_{ij} tensor.

Optical and Electronic Properties. The optical properties were studied using UV−vis diffuse reflectance spectroscopy and PYSA to determine the band gap and valence band energies of the materials, as shown in Figure 5a,b. The experimentally determined band gaps were determined according to the Tauc method[50] and are 2.23(5) eV for $LiCu_3TiS_4$, 1.86(5) eV for $LiCu_3TiSe_4$, and 1.34(5) eV for $LiCu_3TiTe_4$, as shown in Figure S20. The band gap of $LiCu_3TiS_4$ implies that the material should appear yellow in color; however, crystals of this material appear black until ground, at which point a yellow powder is reached. This effect is attributed to both mid-gap states introduced by defects in the structures and to high attenuation of light by the material which will yield darker colors the thicker the sample is. The decrease in the band gap as the chalcogen changes from S to Se and Te is well reported in the literature[51] and can be explained

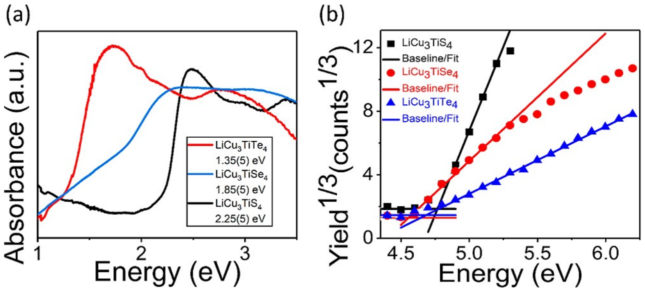

Figure 5. UV−vis absorbance spectra [derived via Kubelka−Munk equation, $F(R) = (1 - R)2/2R$, from diffuse reflectance measurements] of (a) $LiCu_3TiS_4$, $LiCu_3TiSe_4$, and $LiCu_3TiTe_4$. (b) PYSA of $LiCu_3TiS_4$, $LiCu_3TiSe_4$, and $LiCu_3TiTe_4$.

by the increase in the spatial extension of the filled p orbitals, as well as the increase in energy as one goes down group 16. This leads to an increase in the orbital overlap between the chalcogen and the Cu/Ti in the compound, and a decreasing difference in electronegativity between the metals and the Q results in greater bond covalency and larger energy dispersion, which reduces the size of the band gap. This phenomenon is discussed in the following section. Of note is the large tail at the end of the absorption edge of the $LiCu_3TiSe_4$ diffuse reflectance spectra, which we ascribe to the presence of cations and anti-site defect vacancies that produce mid-gap states, leading to sub band gap absorption.

The work functions, which are also essentially the VBM for semiconductors, were obtained by fitting the linear region of the PYSA data[52−55] to determine the linear onset. The work functions were measured to be 4.77(5) eV for $LiCu_3TiS_4$, 4.56(5) eV for $LiCu_3TiSe_4$, and 4.69(5) eV for $LiCu_3TiTe_4$ with respect to vacuum, as shown in Figure 5b. The expected trend in the work function for isostructural compounds when the anions are exchanged moving down a group is that the value decreases because the valence electrons become less bound. This expectation is only true for isostructural comparisons, but values can change with the presence of disorder and anti-site defects such as those mentioned above. As such, the work function for $LiCu_3TiTe_4$ can be expected to deviate slightly from this trend because the structure is distinct, though highly similar to that of the sulfide and selenide analogues. Taking the VBM in conjunction with the band gap yields conduction band minima (CBMs) of 2.54(7) eV for $LiCu_3TiS_4$, 2.70(7) eV for $LiCu_3TiSe_4$, and 3.45(7) eV for $LiCu_3TiTe_4$. Each sample's direct current (DC) electrical resistivity was measured using cold-pressed polycrystalline pellets. The resistivity of the sulfide was determined to be 5×10^3 Ω-cm and 5×10^4 Ω-cm for the selenide and 80 Ω-cm for telluride (see Table 6).

Electronic Band Structure Calculations. The calculations for all compounds were conducted with no site occupancy disorder in the $LiCu_3TiQ_4$ (Q = S and Se) structure type due to the increased computational cost of handling the disorder in the refined structures. The convex hull method[56] within the Open Quantum Materials Database[57,58] was used to evaluate the energetic stability of $LiCu_3TiS_4$, $LiCu_3TiSe_4$, and $LiCu_3TiTe_4$, which were calculated to be stable (i.e., on the hull) at $T = 0$ K. The calculated band dispersion plots (see Figure 6a−c) for all materials predict that they have indirect band gaps with their VBM occurring at the R point and their CBM at the X point. The calculations predict band gaps of ∼1.5 eV for $LiCu_3TiS_4$, ∼1.25 eV for $LiCu_3TiSe_4$, and ∼1 eV for $LiCu_3TiTe_4$. The values for sulfide and selenide were below the experimental values. This result is reasonable because it is well established that band structures calculated using DFT typically underestimate the experimental values.[59]

Table 6. DC Electrical Resistivities, Work Functions, and Optical Band Gaps for $LiCu_3TiQ_4$ (Q = S, Se, and Te)

	$LiCu_3TiS_4$	$LiCu_3TiSe_4$	$LiCu_3TiTe_4$
resistivity (Ω-cm)	5×10^3	5×10^4	80
work function (eV)	4.77(5)	4.56(5)	4.69(5)
bang gap (eV)	2.23(5)	1.86(5)	1.34(5)

The calculated partial density of states (pDOS) for each material is presented alongside the band structure calculations in Figure 6. The calculations predict that the valence band edges in each material mainly comprise Cu 3d orbitals. In contrast, the conduction band predominantly contains Ti 3d orbitals. The placement of the Ti 3d orbitals in the conduction band can be intuited by assigning a 4+ oxidation state to titanium, which gives it a d^0 electron configuration. Analogously, if we assign Cu a 1+ oxidation state, yielding a d^{10} electron configuration, we expect these d orbitals to lie squarely in the valence band, which is in good agreement with the calculated results. Additionally, because the local coordination geometry of both Cu and Ti is tetrahedral, we observe two pronounced peaks in the pDOS for the d orbitals arising from the tetrahedral crystal field splitting. However, the effect is more pronounced for Ti than that for Cu. The Cu d orbitals themselves are dispersed over an energy interval greater than 2 eV for all compounds because they extend over the entire calculated energy range for the valence band. While the Ti d orbitals extend over the entirety of the conduction band, they are comparatively less dispersed than the Cu d orbitals because their dispersion is closer to ∼1 eV. As the chalcogen becomes heavier, we expect to see an increase in the energy dispersion of the Cu and Ti d orbital bands pDOS across the compounds, which is due to the aforementioned increased valence orbital extension.

The partial crystal orbital Hamilton population (COHP) curves for each compound are presented in Figure 6a−c. The average bonding character of the conduction bands in each material is antibonding, with the largest contributions coming from the Cu−Q and Q−Ti combinations. All materials have slight antibonding character, which transitions to bonding ∼1 eV below the valence band edge. The antibonding character of the valence band often motivates materials to develop cation vacancies, which serve to effectively hole dope the material as the removal of electrons from the valence band edge increases the overall bonding character of the compound. The small intermixing of Li and Ti in their Wyckoff sites also implies the formation of anti-site defects, as seen in $LiInSe_2$.[5] The formation of these vacancies and anti-site defects lowers the Fermi level and can produce defect states that fall within the band gap, leading to sub-band gap absorption of light. The large tail observed at the edge of the optical absorption spectra of $LiCu_3TiSe_4$ may thus be potentially rationalized by this phenomenon due to the anti-bonding character present near the valence band top of the compound.

The DFT calculations predict that all compounds have valence bands with dispersions (the change in energy along a particular direction) along $\Gamma \rightarrow R$ being ∼0.25 eV near the maxima. The dispersions near the CBM along the $X \rightarrow M$

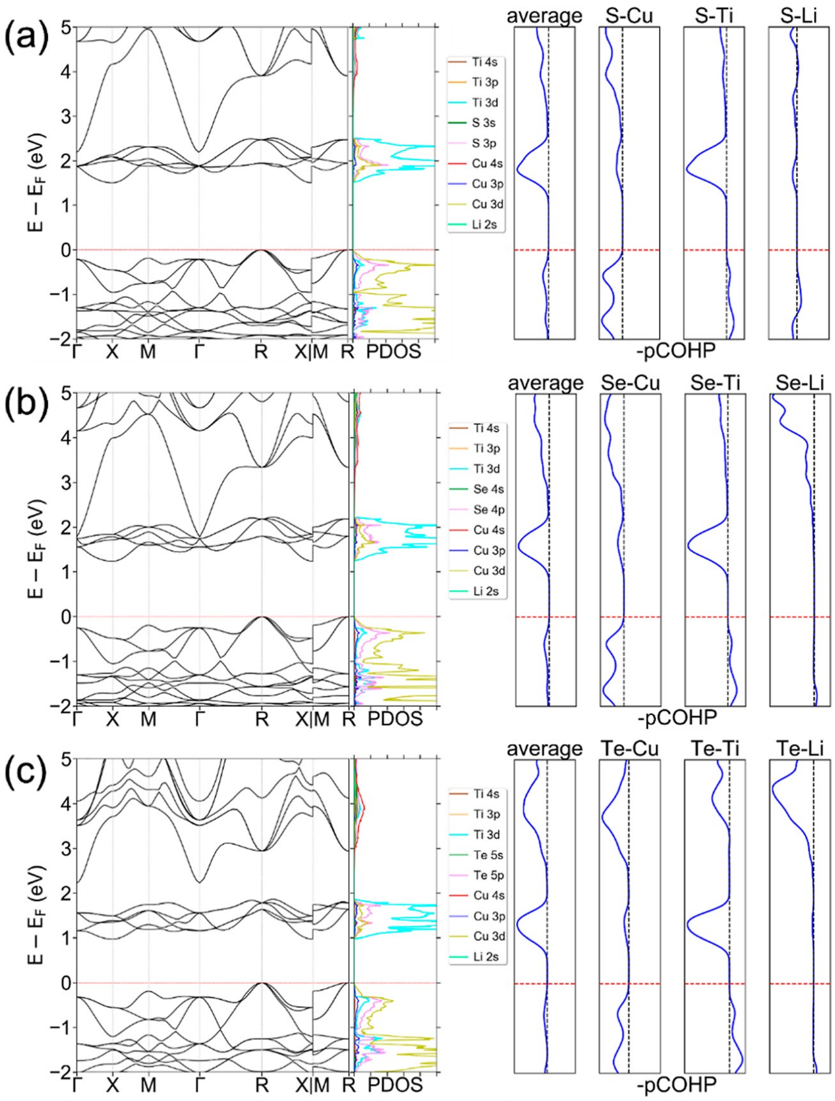

Figure 6. Electronic band structures, pDOS, and partial COHP curves of (a) $LiCu_3TiS_4$, (b) $LiCu_3TiSe_4$, and (c) $LiCu_3TiTe_4$ in the ideal $LiCu_3TiQ_4$ (Q = S and Se) structure. The COHP curves indicate the bonding character of states within a given energy interval. Negative (leftward) values for these curves correspond to antibonding combinations, while positive (rightward) values indicate bonding character. If the curve lies on the centerline, the combinations are non-bonding. The amplitude of the curves depends in part on both the number of states in a given energy interval (i.e., the pDOS) and the extent of orbital overlap.

direction is ~0.25 eV for the sulfide and ~0.2 eV for the selenide and telluride. The electron effective masses near the CBM are 2.737 m_e along $X \rightarrow \Gamma$ and 1.342 m_e along $X \rightarrow M$ for the sulfide, 2.878 m_e along $X \rightarrow \Gamma$ and 1.189 m_e along $X \rightarrow M$ for the selenide, and 2.499 m_e along $X \rightarrow \Gamma$ and 1.375 m_e along $X \rightarrow M$ for the telluride. The hole effective masses near the VBM were 1.057 m_e along $R \rightarrow \Gamma$ and 1.232 m_e along $R \rightarrow X$ for the sulfide, 0.935 m_e along $R \rightarrow \Gamma$ and 1.091 m_e along $R \rightarrow X$ for the selenide, and 0.737 m_e along $R \rightarrow \Gamma$ and 0.863 m_e along $R \rightarrow X$ for the telluride. These predicted dispersions and effective masses suggest that materials should have favorable semiconducting properties, with holes being more mobile than electrons.

The nature of the conduction band in these systems is defined by the empty d orbitals of the titanium atoms. Because the concentration of titanium atoms in the unit cell is ~10% (one in nine atoms in the formula), highly dispersed electronic bands cannot be developed. This gives rise to the relatively high electron effective masses in the systems. On the other hand, the nature of the valence bands is defined by the filled d orbitals of Cu and p orbital states of S atoms, giving rise to rather broad energy dispersions and consequently lower affected masses.

The predicted phonon dispersion relations and partial densities of states for $LiCu_3TiQ_4$ (Q = S, Se, and Te) are presented in Figure S21a−c. The phonon dispersion relation and pDOS for $LiCu_3TiTe_4$ were calculated using the compound in the $LiCu_3TiQ_4$ (Q = S and Se) structure, owing to the computational cost of modeling the disorder in the structure solved by single-crystal X-ray diffraction. The phonon dispersion relations have no imaginary frequencies, which indicates that all three structures are dynamically stable at $T = 0$ K.

■ CONCLUSIONS

The three lithium copper chalcotitanates together establish a new stuffed diamond structure type. The compounds are semiconductors with band gaps of 2.23(5), 1.86(5), and

1.34(5) eV with low hole carrier effective masses, which opens new opportunities for future investigations of a broad variety of physical and optoelectronic properties. The formation of $LiCu_3TiTe_4$ proceeds through three separate intermediate phases before forming. The staggered order and appearance of the intermediate phases in relation to $LiCu_3TiTe_4$ suggest that its formation may occur in a stepwise fashion, with one intermediate phase leading to another. Their structures can be understood as hybrids between the zinc-blende structure and the sulvanite structure. We rationalize the formation of the stuffed diamond-type structure because the charge-balanced formula requires five cations and only four anions. Given the strong preferences of Li^+ and Cu^+ for tetrahedral coordination, the diamond-type structure (zinc blende), which requires an equal number of cations and anions, is strongly favored. The compounds solve this conundrum by accommodating the extra tetrahedral cations in the voids available in the diamond structure. This insight and the examples of other stuffed aristotype structures mentioned in the introduction for a variety of chemical classes imply that the stuffing of aristotype structures using the same principle may be possible if they have available voids. Therefore, it could be an attractive material design attribute that could be used for targeted material discovery.

■ ASSOCIATED CONTENT

Supporting Information

The Supporting Information is available free of charge at https://pubs.acs.org/doi/10.1021/jacs.2c03501.

Additional experimental details, SEM/EDX, PXRD, DTA, Tauc plots, phonon dispersions, and PDOS (PDF)

Accession Codes

CCDC 2163868−2163870 contain the supplementary crystallographic data for this paper. These data can be obtained free of charge via www.ccdc.cam.ac.uk/data_request/cif, or by emailing data_request@ccdc.cam.ac.uk, or by contacting The Cambridge Crystallographic Data Centre, 12 Union Road, Cambridge CB2 1EZ, UK; fax: +44 1223 336033.

■ AUTHOR INFORMATION

Corresponding Author

Mercouri G. Kanatzidis − *Department of Chemistry, Northwestern University, Evanston, Illinois 60208, United States;* orcid.org/0000-0003-2037-4168; Email: m-kanatzidis@northwestern.edu

Authors

Michael A. Quintero − *Department of Chemistry, Northwestern University, Evanston, Illinois 60208, United States;* orcid.org/0000-0002-0709-1676

Jiahong Shen − *Department of Materials Science and Engineering, Northwestern University, Evanston, Illinois 60208, United States;* orcid.org/0000-0002-1951-2183

Craig C. Laing − *Department of Chemistry, Northwestern University, Evanston, Illinois 60208, United States;* orcid.org/0000-0002-0654-4741

Christopher Wolverton − *Department of Materials Science and Engineering, Northwestern University, Evanston, Illinois 60208, United States;* orcid.org/0000-0003-2248-474X

Complete contact information is available at: https://pubs.acs.org/10.1021/jacs.2c03501

Notes

The authors declare no competing financial interest.

■ ACKNOWLEDGMENTS

This synthesis and material characterization study was supported by the National Science Foundation through grant DMR-2003476. This study made use of IMSERC at the Northwestern University, which has received support from the Soft and Hybrid Nanotechnology Experimental (SHyNE) Resource (NSF ECCS-1542205), the State of Illinois, and IIN. This study used the EPIC facility of Northwestern University's NUANCE Center, which has received support from the SHyNE Resource (NSF ECCS-2025633), the IIN, and the Northwestern MRSEC program (NSF DMR-1720139).

■ REFERENCES

(1) Thackeray, M. M.; Wolverton, C.; Isaacs, E. D. Electrical Energy Storage for Transportation—Approaching the Limits of, and Going Beyond, Lithium-Ion Batteries. *Energy Environ. Sci.* **2012**, *5*, 7854−7863.

(2) Caruso, A. N. The Physics of Solid-State Neutron Detector Materials and Geometries. *J. Phys.: Condens. Matter* **2010**, *22*, 443201.

(3) Kim, T.; Song, W.; Son, D.-Y.; Ono, L. K.; Qi, Y. Lithium-Ion Batteries: Outlook on Present, Future, and Hybridized Technologies. *J. Mater. Chem. A* **2019**, *7*, 2942−2964.

(4) Chica, D. G.; He, Y.; McCall, K. M.; Chung, D. Y.; Pak, R. O.; Trimarchi, G.; Liu, Z.; De Lurgio, P. M.; Wessels, B. W.; Kanatzidis, M. G. Direct Thermal Neutron Detection by the 2d Semiconductor 6liinp2se6. *Nature* **2020**, *577*, 346−349.

(5) Guo, L.; Xu, Y.; Zheng, H.; Xue, W.; Dong, J.; Zhang, B.; He, Y.; Zha, G.; Chung, D. Y.; Jie, W.; Kanatzidis, M. G. Stoichiometric Effects on the Photoelectric Properties of Liinse2 Crystals for Neutron Detection. *Cryst. Growth Des.* **2018**, *18*, 2864−2870.

(6) Graf, T.; Felser, C.; Parkin, S. S. P. Simple Rules for the Understanding of Heusler Compounds. *Prog. Solid State Chem.* **2011**, *39*, 1−50.

(7) Liu, Z. K.; Yang, L. X.; Wu, S.-C.; Shekhar, C.; Jiang, J.; Yang, H. F.; Zhang, Y.; Mo, S.-K.; Hussain, Z.; Yan, B.; Felser, C.; Chen, Y. L. Observation of Unusual Topological Surface States in Half-Heusler Compounds Lnptbi (Ln=Lu, Y). *Nat. Commun.* **2016**, *7*, 12924.

(8) Pavlosiuk, O.; Kaczorowski, D.; Wiśniewski, P. Shubnikov - De Haas Oscillations, Weak Antilocalization Effect and Large Linear Magnetoresistance in the Putative Topological Superconductor Lupdbi. *Sci. Rep.* **2015**, *5*, 9158.

(9) Goll, G.; Marz, M.; Hamann, A.; Tomanic, T.; Grube, K.; Yoshino, T.; Takabatake, T. Thermodynamic and Transport Properties of the Non-Centrosymmetric Superconductor Labipt. *Phys. B* **2008**, *403*, 1065−1067.

(10) Butch, N. P.; Syers, P.; Kirshenbaum, K.; Hope, A. P.; Paglione, J. Superconductivity in the Topological Semimetal Yptbi. *Phys. Rev. B: Condens. Matter Mater. Phys.* **2011**, *84*, 220504.

(11) Tafti, F. F.; Fujii, T.; Juneau-Fecteau, A.; René de Cotret, S.; Doiron-Leyraud, N.; Asamitsu, A.; Taillefer, L. Superconductivity in the Noncentrosymmetric Half-Heusler Compound Luptbi: A Candidate for Topological Superconductivity. *Phys. Rev. B: Condens. Matter Mater. Phys.* **2013**, *87*, 184504.

(12) Pan, Y.; Nikitin, A. M.; Bay, T. V.; Huang, Y. K.; Paulsen, C.; Yan, B. H.; de Visser, A. Superconductivity and Magnetic Order in the Noncentrosymmetric Half-Heusler Compound Erpdbi. *EPL* **2013**, *104*, 27001.

(13) Joshi, G.; He, R.; Engber, M.; Samsonidze, G.; Pantha, T.; Dahal, E.; Dahal, K.; Yang, J.; Lan, Y.; Kozinsky, B.; Ren, Z. Nbfesb-Based P-Type Half-Heuslers for Power Generation Applications. *Energy Environ. Sci.* **2014**, *7*, 4070−4076.

(14) Zou, M.; Li, J.-F.; Guo, P.; Kita, T. Synthesis and Thermoelectric Properties of Fine-Grained Fevsb System Half-

Heusler Compound Polycrystals with High Phase Purity. *J. Phys. D: Appl. Phys.* **2010**, *43*, 415403.

(15) Yan, X.; Liu, W.; Chen, S.; Wang, H.; Zhang, Q.; Chen, G.; Ren, Z. Thermoelectric Property Study of Nanostructured P-Type Half-Heuslers (Hf, Zr, Ti) Cosb0. 8sn0. 2. *Adv. Energy Mater.* **2013**, *3*, 1195−1200.

(16) Landrum, G. A.; Hoffmann, R.; Evers, J.; Boysen, H. The Tinisi Family of Compounds: Structure and Bonding. *Inorg. Chem.* **1998**, *37*, 5754−5763.

(17) Kaczorowski, D.; Leithe-Jasper, A.; Rogl, P.; Flandorfer, H.; Cichorek, T.; Pietri, R.; Andraka, B. Magnetic, Thermodynamic, and Electrical Transport Properties of Ternary Equiatomic Ytterbium Compounds Yb Tm (T= Transition Metal, M= Sn and Bi). *Phys. Rev. B: Condens. Matter Mater. Phys.* **1999**, *60*, 422.

(18) Morozkin, A. V.; Nikitin, S. A.; Seropegin, Y. D.; Sviridov, I. A.; Tskhadadze, I. A. Structural and Magnetic Properties of New Rruge Compounds. *J. Alloys Compd.* **1998**, *268*, L1−L2.

(19) Canepa, F.; Palenzona, A.; Cirafici, S.; Merlo, F. Physical Properties of Gdniga. *J. Alloys Compd.* **1998**, *279*, L11−L12.

(20) Merlo, F.; Fornasini, M. L.; Cirafici, S.; Canepa, F. Physical Properties of Gdniin. *J. Alloys Compd.* **1998**, *267*, L12−L13.

(21) Mewis, A. Caagp Und Caagas-Zwei Verbindungen Mit Fe2p-Struktur/Caagp and Caagas-Two Compounds with the Fe2p-Structure. *Z. Naturforsch. B Chem. Sci.* **1979**, *34*, 14−17.

(22) Stegmaier, S.; Fässler, T. F. Lithium-Stuffed Diamond Polytype Zn−Tt Structures (Tt= Sn, Ge): The Two Lithium−Zinc−Tetrelides Li3zn2sn4 and Li2znge3. *Inorg. Chem.* **2013**, *52*, 2809−2816.

(23) Henze, A.; Hlukhyy, V.; Fässler, T. F. Fully and Partially Li-Stuffed Diamond Polytypes with Ag−Ge Structures: Li2agge and Li2. 53agge2. *Inorg. Chem.* **2015**, *54*, 1152−1158.

(24) Pauling, L.; Hultgren, R. The Crystal Structure of Sulvanite, Cu_3vs_4. *Z. Kristallogr. Cryst. Mater.* **1933**, *84*, 204−212.

(25) Ikeda, S.; Aono, N.; Iwase, A.; Kobayashi, H.; Kudo, A. Cu3ms4 (M= V, Nb, Ta) and Its Solid Solutions with Sulvanite Structure for Photocatalytic and Photoelectrochemical H2 Evolution under Visible-Light Irradiation. *ChemSusChem* **2019**, *12*, 1977−1983.

(26) Takayama, T.; Tsuji, I.; Aono, N.; Harada, M.; Okuda, T.; Iwase, A.; Kato, H.; Kudo, A. Development of Various Metal Sulfide Photocatalysts Consisting of D0, D5, and D10 Metal Ions for Sacrificial H2 Evolution under Visible Light Irradiation. *Chem. Lett.* **2017**, *46*, 616−619.

(27) Liu, X.-P.; Feng, Z.-Z.; Guo, S.-P.; Xia, Y.; Zhang, Y. Promising Thermoelectric Materials of Cu3vx4 (X= S, Se, Te): A Cu-Vx Framework Plus Void Tunnels. *Int. J. Mod. Phys. C* **2019**, *30*, 1950045.

(28) Wen, J.; Huang, H.; Yu, X.; Wang, D.; Guo, K.; Wan, D.; Luo, J.; Zhao, J.-T. Thermoelectric Properties of P-Type Cu3vse4 with High Seebeck Coefficients. *J. Alloys Compd.* **2021**, *879*, 160387.

(29) Haque, E. Outstanding Thermoelectric Performance of Mcu3x4 (M= V, Nb, Ta; X= S, Se, Te) with Unaffected Band Degeneracy under Pressure. *ACS Appl. Energy Mater.* **2021**, *4*, 1942−1953.

(30) Koley, B.; Lakshan, A.; Raghuvanshi, P. R.; Singh, C.; Bhattacharya, A.; Jana, P. P. Ultralow Lattice Thermal Conductivity at Room Temperature in Cu 4 TiSe 4. *Angew. Chem., Int. Ed.* **2021**, *60*, 9106−9113.

(31) Khoury, J. F.; Hao, S.; Stoumpos, C. C.; Yao, Z.; Malliakas, C. D.; Aydemir, U.; Slade, T. J.; Snyder, G. J.; Wolverton, C.; Kanatzidis, M. G. Quaternary Pavonites A1+ X Sn2−X Bi5+ X S10 (a+= Li+, Na +): Site Occupancy Disorder Defines Electronic Structure. *Inorg. Chem.* **2018**, *57*, 2260−2268.

(32) Baláž, M.; Zorkovská, A.; Urakaev, F.; Baláž, P.; Briančin, J.; Bujňáková, Z.; Achimovičová, M.; Gock, E. Ultrafast Mechanochemical Synthesis of Copper Sulfides. *RSC Adv.* **2016**, *6*, 87836−87842.

(33) Hohenberg, P.; Kohn, W. Inhomogeneous Electron Gas. *Phys. Rev.* **1964**, *136*, B864.

(34) Kohn, W.; Sham, L. J. Self-Consistent Equations Including Exchange and Correlation Effects. *Phys. Rev.* **1965**, *140*, A1133.

(35) Kresse, G.; Furthmüller, J. Efficiency of Ab-Initio Total Energy Calculations for Metals and Semiconductors Using a Plane-Wave Basis Set. *Comput. Mater. Sci.* **1996**, *6*, 15−50.

(36) Kresse, G.; Furthmüller, J. Efficient Iterative Schemes for Ab Initio Total-Energy Calculations Using a Plane-Wave Basis Set. *Phys. Rev. B: Condens. Matter Mater. Phys.* **1996**, *54*, 11169.

(37) Blöchl, P. E. Projector Augmented-Wave Method. *Phys. Rev. B: Condens. Matter Mater. Phys.* **1994**, *50*, 17953.

(38) Perdew, J. P.; Burke, K.; Ernzerhof, M. Generalized Gradient Approximation Made Simple. *Phys. Rev. Lett.* **1996**, *77*, 3865.

(39) Kresse, G.; Joubert, D. From Ultrasoft Pseudopotentials to the Projector Augmented-Wave Method. *Phys. Rev. B: Condens. Matter Mater. Phys.* **1999**, *59*, 1758.

(40) Togo, A.; Tanaka, I. First Principles Phonon Calculations in Materials Science. *Scr. Mater.* **2015**, *108*, 1−5.

(41) McClain, R.; Malliakas, C. D.; Shen, J.; He, J.; Wolverton, C.; González, G. B.; Kanatzidis, M. G. Mechanistic Insight of Kbiq 2 (Q= S, Se) Using Panoramic Synthesis Towards Synthesis-by-Design. *Chem. Sci.* **2021**, *12*, 1378−1391.

(42) Haynes, A. S.; Stoumpos, C. C.; Chen, H.; Chica, D.; Kanatzidis, M. G. Panoramic Synthesis as an Effective Materials Discovery Tool: The System Cs/Sn/P/Se as a Test Case. *J. Am. Chem. Soc.* **2017**, *139*, 10814−10821.

(43) Shoemaker, D. P.; Hu, Y.-J.; Chung, D. Y.; Halder, G. J.; Chupas, P. J.; Soderholm, L.; Mitchell, J. F.; Kanatzidis, M. G. In Situ Studies of a Platform for Metastable Inorganic Crystal Growth and Materials Discovery. *Proc. Natl. Acad. Sci. U.S.A.* **2014**, *111*, 10922−10927.

(44) McClain, R.; Malliakas, C. D.; Shen, J.; Wolverton, C.; Kanatzidis, M. G. In Situ Mechanistic Studies of Two Divergent Synthesis Routes Forming the Heteroanionic Biocuse. *J. Am. Chem. Soc.* **2021**, *143*, 12090−12099.

(45) Toby, B. H.; Von Dreele, R. B. Gsas-Ii: The Genesis of a Modern Open-Source All Purpose Crystallography Software Package. *J. Appl. Crystallogr.* **2013**, *46*, 544−549.

(46) Buehrer, W.; Altorfer, F.; Mesot, J.; Bill, H.; Carron, P.; Smith, H. G. Lattice Dynamics and the Diffuse Phase Transition of Lithium Sulphide Investigated by Coherent Neutron Scattering. *J. Phys.: Condens. Matter* **1991**, *3*, 1055.

(47) Cunningham, P. T.; Johnson, S. A.; Cairns, E. J. Phase Equilibria in Lithium-Chalcogen Systems. *J. Electrochem. Soc.* **1971**, *118*, 1941.

(48) Zintl, E.; Harder, A.; Dauth, B. Gitterstruktur Der Oxyde Sulfide, Selenide Und Telluride Des Lithiums, Natriums Und Kaliums. *Z. Elektrochem. angew. phys. Chem.* **1934**, *40*, 588−593.

(49) Bindi, L.; Carbone, C.; Belmonte, D.; Cabella, R.; Bracco, R. Weissite from Gambatesa Mine, Val Graveglia, Liguria, Italy: Occurrence, Composition and Determination of the Crystal Structure. *Mineral. Mag.* **2013**, *77*, 475−483.

(50) Makuła, P.; Pacia, M.; Macyk, W. How to Correctly Determine the Bandgap Energy of Modified Semiconductor Photocatalysts Based on Uv−Vis Spectra. *J. Phys. Chem. Lett.* **2018**, *9*, 6814−6817.

(51) Johnsen, S.; Peter, S. C.; Nguyen, S. L.; Song, J.-H.; Jin, H.; Freeman, A. J.; Kanatzidis, M. G. $Tl_2Hg_3Q_4$ (Q= S, Se, and Te): High-Density, Wide-Band-Gap Semiconductors. *Chem. Mater.* **2011**, *23*, 4375−4383.

(52) Harwell, J. R.; Baikie, T. K.; Baikie, I. D.; Payne, J. L.; Ni, C.; Irvine, J. T. S.; Turnbull, G. A.; Samuel, I. D. W. Probing the Energy Levels of Perovskite Solar Cells Via Kelvin Probe and Uv Ambient Pressure Photoemission Spectroscopy. *Phys. Chem. Chem. Phys.* **2016**, *18*, 19738−19745.

(53) Yamashita, D.; Ishizaki, A. In Situ Measurements of Change in Work Function of Pt, Pd and Au Surfaces During Desorption of Oxygen by Using Photoemission Yield Spectrometer in Air. *Appl. Surf. Sci.* **2016**, *363*, 240−244.

(54) He, Y.; Stoumpos, C. C.; Hadar, I.; Luo, Z.; McCall, K. M.; Liu, Z.; Chung, D. Y.; Wessels, B. W.; Kanatzidis, M. G. Demonstration of Energy-Resolved Γ-Ray Detection at Room Temperature by the

Cspbcl3 Perovskite Semiconductor. *J. Am. Chem. Soc.* **2021**, *143*, 2068−2077.

(55) Hadar, I.; Hu, X.; Luo, Z.-Z.; Dravid, V. P.; Kanatzidis, M. G. Nonlinear Bandgap Tunability in Selenium−Tellurium Alloys and Its Utilization in Solar Cells. *ACS Energy Lett.* **2019**, *4*, 2137−2143.

(56) Barber, C. B.; Dobkin, D. P.; Huhdanpaa, H. The Quickhull Algorithm for Convex Hulls. *ACM Trans. Math Software* **1996**, *22*, 469−483.

(57) Saal, J. E.; Kirklin, S.; Aykol, M.; Meredig, B.; Wolverton, C. Materials Design and Discovery with High-Throughput Density Functional Theory: The Open Quantum Materials Database (Oqmd). *Jom* **2013**, *65*, 1501−1509.

(58) Kirklin, S.; Saal, J. E.; Meredig, B.; Thompson, A.; Doak, J. W.; Aykol, M.; Rühl, S.; Wolverton, C. The Open Quantum Materials Database (Oqmd): Assessing the Accuracy of Dft Formation Energies. *npj Comput. Mater.* **2015**, *1*, 15010.

(59) Zunger, A. Beware of Plausible Predictions of Fantasy Materials. *Nature* **2019**, *566*, 447−449.

https://doi.org/10.1021/jacs.2c03501